Dalton Transactions

ROYAL SOCIETY OF CHEMISTRY

PAPER

View Article Online
View Journal | View Issue

Cite this: *Dalton Trans.*, 2023, **52**, 16224

Controlled synthesis of photoresponsive bismuthinite (Bi_2S_3) nanostructures mediated through a new 1D bismuth-pyrimidylthiolate coordination polymer as a molecular precursor†

Atharva Yeshwant Kulkarni,‡[a] Gourab Karmakar, ‡[b,c] Alpa Y. Shah,[b] Sandeep Nigam, [b,c] Gayatri Kumbhare,[a] Adish Tyagi, *[b,c] Raymond J. Butcher,[d] Rohit Singh Chauhan *[a] and N. Naveen Kumar[e]

Bismuthinite (Bi_2S_3) nanostructures have garnered significant interest due to their appealing photoresponsivity which has positioned them as an attractive choice for energy conversion applications. However, to utilize their full potential, a simple and economically viable method of preparation is highly desirable. Herein, we present the synthesis and characterization including structural elucidation of a new air- and moisture-stable bismuth-pyrimidylthiolate complex. This complex serves as an efficient single-source molecular precursor for the facile preparation of phase-pure Bi_2S_3 nanostructures. Powder X-ray diffraction (PXRD), Raman spectroscopy, electron dispersive spectroscopy (EDS) and electron microscopy techniques were used to assess the crystal structure, phase purity, elemental composition and morphology of the as-prepared nanostructures. This study also revealed the profound effects of temperature and growth duration on the crystallinity, phase formation and morphology of nanostructures. The optical band gap of the nanostructures was tuned within the range of 1.9–2.3 eV, which is blue shifted with respect to the bulk bandgap and suitable for photovoltaic applications. Liquid junction photo-electrochemical cells fabricated from the as-prepared Bi_2S_3 nanostructure exhibit efficient photoresponsivity and good photo-stability, which project them as promising candidates for alternative low-cost photon absorber materials.

Received 7th July 2023,
Accepted 8th September 2023

DOI: 10.1039/d3dt02143b

rsc.li/dalton

Introduction

The ever growing global energy crisis and the pressing need for environmental governance have intensified the quest for sustainable and efficient solar energy conversion technologies. Photovoltaic cells play a pivotal role in this direction.[1] Developing efficient solar absorber materials which constitute the heart of solar cells is currently an important research area. In this context, metal chalcogenides offer a fertile chemical space for exploration.[2] While commercialized materials like $Cu_2(In, Ga)Se_2$ and CdTe have shown promise, challenges such as scarcity, toxicity, and structural complexities necessitate the exploration of alternative chalcogenides.[3] Recently, group-V metal chalcogenides (V–VI materials), particularly bismuthinite (Bi_2S_3), have emerged as promising photon absorber materials due to their exciting electrical and optical properties. Bismuthinite possesses several key attributes such as a narrow band gap, a high absorption coefficient of the order 10^5 cm^{-1} and good carrier mobility, which make it an intriguing material for energy conversion applications.[4] Bi_2S_3 is stibnite-structured and crystallizes in the orthorhombic P_{nma} space group and can be described as a layered structure which offers the opportunity for exfoliation down to a monolayer.[5] With a band gap ranging from 1.4 to 1.7 eV, Bi_2S_3 holds potential for generating high open-circuit voltage, making it an attractive light absorber material for top cells in tandem solar cells. Furthermore, due to the restriction of complaints about hazardous substances and benefiting from non-toxic and Earth-abundant constituent elements, Bi_2S_3 serves as a promising candidate for sustainable solar cells.[6]

[a]*Department of Chemistry, K. J. Somaiya College of Science and Commerce, Vidyavihar, Mumbai 400077, India. E-mail: rohit.chauhan@somaiya.edu*
[b]*Chemistry Division, Bhabha Atomic Research Centre, Mumbai 400085, India. E-mail: tyagia@barc.gov.in*
[c]*Homi Bhabha National Institute, Anushaktinagar, Mumbai-400094, India*
[d]*Department of Chemistry, Howard University, Washington, DC, 20059, USA*
[e]*Materials Science Division, Bhabha Atomic Research Centre, Mumbai-400085, India*

†Electronic supplementary information (ESI) available: Additional figures *etc.* CCDC 2210360 for $[Bi(4,6\text{-}Me_2pymS)_3]_n$. For ESI and crystallographic data in CIF or other electronic format see DOI: https://doi.org/10.1039/d3dt02143b

‡These authors contributed equally to this work.

To fully exploit the potential of Bi_2S_3 in solar cell applications, a cost-effective and scalable synthetic protocol for nanometric Bi_2S_3 is highly desirable. Various solution-assisted and solventless synthetic routes including solvothermal,[7] hydrothermal,[8] sonochemical,[9] microwave-assisted,[10] green synthesis,[11] *etc*., have been explored for the synthesis of Bi_2S_3 nanostructures. It is observed that most of these methods employ a dual precursor route wherein a bismuth source ($Bi(NO_3)_3{\cdot}5H_2O$, BiI_3, *etc*.) combines with a suitable sulfur source (elemental S, H_2S, Na_2S, thiourea, hexamethyldisilathiane, *etc*.) to produce Bi_2S_3. However, the dual precursor route often employs precursors which are either sensitive (BiI_3, Na_2S, and hexamethyldisilathiane) or toxic (H_2S), which severely limits the wide-scale utility of the final material.[12] In light of the limitations associated with the dual precursor route, a single-source precursor (SSP) has gained significant attraction. The SSP route involves a precursor molecule that contains all the desired constituent elements with preformed bonds between them. This approach ensures a low decomposition temperature, phase purity of the final product and high reproducibility of experimental results.[12] Moreover, molecular precursors offer several distinct advantages over the dual precursor route in terms of lower defect concentrations and better control over their morphology and electronic properties.[13] These appealing features of SSPs coupled with the promising applications of Bi_2S_3 have ignited extensive research for the development of SSPs for Bi_2S_3. However, only a few suitable precursors have been identified and that too they are mainly derived from xanthates, dithiocarbamates and dithiophosphates.[13–22] In recent times, coordination polymers have gained significant attention as versatile SSPs, enabling the synthesis of advanced materials with unique morphologies that are hard to realize in conventional synthetic methods.[23,24] The coordination polymer allows controlled release of the constituent elements during thermal decomposition which provides access to nanomaterials of uniform size and morphology. As a result of this, when thermolyzed under appropriate conditions, they convert into materials with unusual morphology and chemical compositions. Moreover, due to the porous nature of the coordination polymers, they sometimes retain the structural exoskeleton after decomposition, which leads to porous nanomaterials with distinctive properties in several cases.[23] The most distinctive feature of coordination polymers is the possibility of tuning their thermal stability with the choice of metal ions/clusters and linkers. Consequently, various functional nanomaterials/composites and heterostructures can be obtained depending on the nature of the precursor and decomposition conditions.[23] Depending on the countless number and types of coordination polymers, decomposition routes, reaction times, media *etc*., a plethora of different nanomaterials/composites/heterostructures can be isolated.[24] Thus, this field offers limitless potential for synthesizing assorted functional nanomaterials for energy and environmental applications. However, surprisingly, coordination polymer-driven synthesis of Bi_2S_3 largely remains elusive.

Considering the importance of SSPs for Bi_2S_3 and continuing our ongoing endeavour towards developing novel precursors for functional metal chalcogenide nanostructures,[25–28] in this report, we present a 1D bismuth-pyrimidylthiolate coordination polymer, which served as an efficient precursor for the synthesis of Bi_2S_3 nanorods. For the preparation of the coordination polymer, we employed an internally functionalized hemilabile 4,6-dimethylpyrimidyl-2-thiolate ligand. Steric congestion exerted by the two hanging methyl groups compels the pyrimidyl thiolate rings to adopt different coordination behaviours *viz*. chelating as well as bridging. This intriguing structural feature assists in the growth of a 1D-polymeric chain of the complex. Furthermore, the thermal transformation of this complex into nanostructures and variations in their crystallinity, morphology and bandgap as a function of reaction time and temperature have been investigated. In this work, it has also been demonstrated that the utilization of this precursor offers a robust synthetic pathway for the formation of highly photoresponsive Bi_2S_3 nanostructures. The results of this work are described herein.

Results and discussion

Synthesis and X-ray crystallography

Treatment of $Bi(NO_3)_3{\cdot}5H_2O$ with the thiolate ligand 4,6-Me_2pymS^- in a 1 : 3 molar ratio resulted in the title complex **1** (Scheme 1). The crystalline complex was characterized by PXRD analysis at room temperature to understand its phase purity (Fig. 1). The reflections match exactly with the simulated PXRD pattern of the complex generated from single crystal

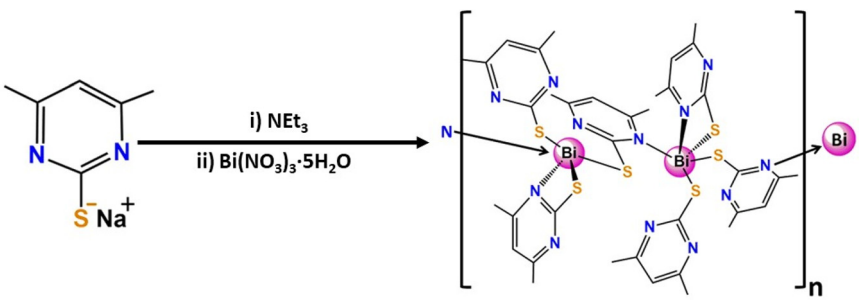

Scheme 1 Schematic diagram for the synthesis of $[Bi(4,6\text{-}Me_2pymS)_3]_n$ (**1**).

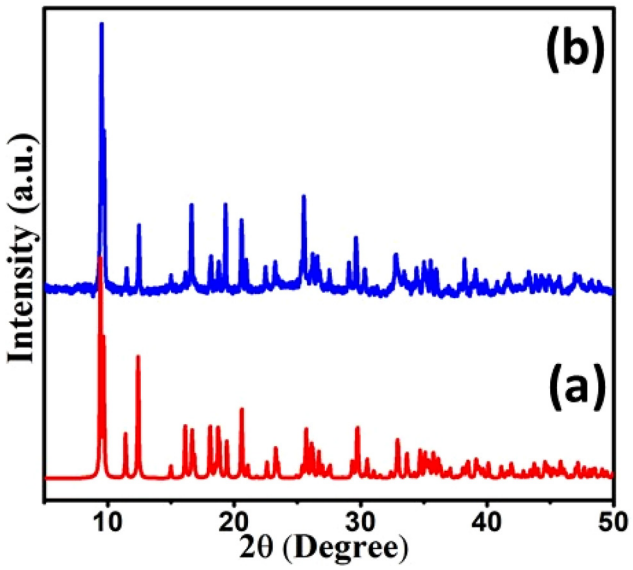

Fig. 1 (a) Simulated XRD pattern of $[Bi(4,6\text{-}Me_2pymS)_3]_n$ (**1**) generated from single crystal data and (b) powder X-ray diffraction (PXRD) pattern of $[Bi(4,6\text{-}Me_2pymS)_3]_n$ (**1**).

data. Diffraction-quality single crystals of the title complex were obtained by the slow evaporation of solvent from the reaction mixture. The molecular structure of complex $[Bi(4,6\text{-}Me_2pymS)_3]_n$ (**1**) with the atomic numbering scheme is shown in Fig. 1a. Crystallographic and structural determination data along with the refinement parameters are given in Table 1 and the selected inter-atomic parameters are summarized in ESI Table 1.†

Table 1 Crystallographic and structural determination data for $[Bi(4,6\text{-}Me_2pymS)_3]_n$ (**1**)

Complex	$[Bi(4,6\text{-}Me_2pymS)_3]_n$
Chemical formula	$C_{18}H_{21}N_6S_3Bi$
Formula weight	626.57
Crystal size (mm^3)	0.1 × 0.05 × 0.025
Temperature/K	100(2)
Wavelength (Å)	0.41328
Crystal system	Orthorhombic
Space group	$P2_12_12_1$
Unit cell dimensions	
a (Å)	10.9192(3)
b (Å)	10.9751(3)
c (Å)	18.2572(5)
α (°)	90
β (°)	90
γ (°)	90
Volume ($Å^3$)	2187.93 (10)
ρ_{calcd} (Mg m^{-3})	1.902
Z	4
μ (mm^{-1})/F(000)	2.086/1208
Limiting indices	$-19 \le h \le 19$ $-15 \le k \le 15$ $-32 \le l \le 32$
Θ for data collection (°)	1.530–22.831
No. of reflections collected	70 021
No. of independent reflections (R_{int})	11 465(0.0510)
Data/restraints/parameters	11 465/0/260
Final R_1, wR_2 indices [$I > 2\sigma I$]	0.0157, 0.0352
R_1, wR_2 (all data)	0.0159, 0.0352
Goodness of fit on F^2	1.044

The title complex **1** crystallizes in a toluene–methanol mixture with an orthorhombic crystal system having the space group $P2_12_12_1$. The asymmetric unit consists of one Bi(III) and three ligand units and the unit cell contains four such molecules ($Z = 4$). The solid-state structure of **1** reveals it to be a 1D coordination polymer, the construction of which is realized by the assembly of the asymmetric unit $[Bi(4,6\text{-}Me_2pymS)_3]$ (Fig. 2a). The structure comprises one-dimensional polymeric wavy chains of the repeating unit $[Bi(4,6\text{-}Me_2pymS)_3]$ propagating through the crystallographic *b*-axis (Fig. 2b). Interestingly the coordination behaviour of the three ligand moieties to the Bi centre differs. While one of the pyrimidine rings is attached to Bi in a chelated fashion through exocyclic sulfur S(1A) and nitrogen N(2A) atoms in a κ-N,S fashion, forming one four-membered metallacyclic ring, another ligand coordinates to the central metal ion through the sulfur atom only (S1B), *i.e.*, in a non-chelating manner. The third ligand exhibits a peculiar bridging behaviour, where it binds with one Bi centre through its sulfur donor site (S1C), whereas the nitrogen N(2C) atom of the ligand coordinates to the Bi atom of another asymmetric unit. This differential bonding fashion of the three ligands leads to a 1D $[Bi(\kappa\text{-}S,N\text{-}pymS)(pymS)(\mu\text{-}S,N\text{-}pymS)]_n$ polymeric chain. These 1D chain assemblies are held in the 3D structure through a complex network of short contacts as presented in Fig. 2c. The central metal ion adopts a distorted square pyramidal geometry where the coordination core is defined through "S3N" donor atoms. One of the reasons for the distortion in the geometry is the presence of a stereochemically active lone pair on bismuth. The sulfur atom S1A resides at the axial position, whereas the equatorial position is occupied by the two non-chelating ligands through sulfur (S1B and S1C) and nitrogen (N(2A) and N(2C)) atoms. The bond angles S(1A)–Bi–S(1B) = 79.46(15), S(1B)–Bi–S(1C) = 87.758(15), S(1C)–Bi–S(1A) = 87.168(16), and N(2A)–Bi–S(1A) = 58.98(3) deviate from the ideal value of 90° which can be considered an important factor contributing to the distortion from the ideal geometry. Another important reason for the distortion is the steric effect rendered by the presence of two methyl groups in each pyrimidyl ring. These types of tris-pyridyl/pyrimidyl chalcogenolate complexes of bismuth, *viz.*, $Bi(Sepy)_3$ and $Bi\{Sepy(Me\text{-}3)\}_3$, have previously been reported.[29] However, due to no or negligible steric interference, these complexes adopt a monomeric structure. In the present case, it would be reasonable to assume that the bulky nature of the ligands compels the third ligand to connect to two neighbouring Bi centres to finally yield a 1D coordination polymer. A similar type of polymeric Bi(III) chalcogenolate complex containing a pyridyl moiety, $[Bi(\kappa^2\text{-}S,N\text{-}pyS)_2(\mu\text{-}S,N\text{-}pyS)]$, can also be found in the literature.[30]

The axial Bi–S bond distance Bi–S(1A) = 2.5837 Å is comparable to reported values, whereas the equatorial Bi–S(1B) and Bi–S(1C) distances are elongated compared to the axial ones. This kind of feature can be observed in other complexes as well.[26,29,31] The Bi–N(2A) bond distance 2.7526(17) Å is signifi-

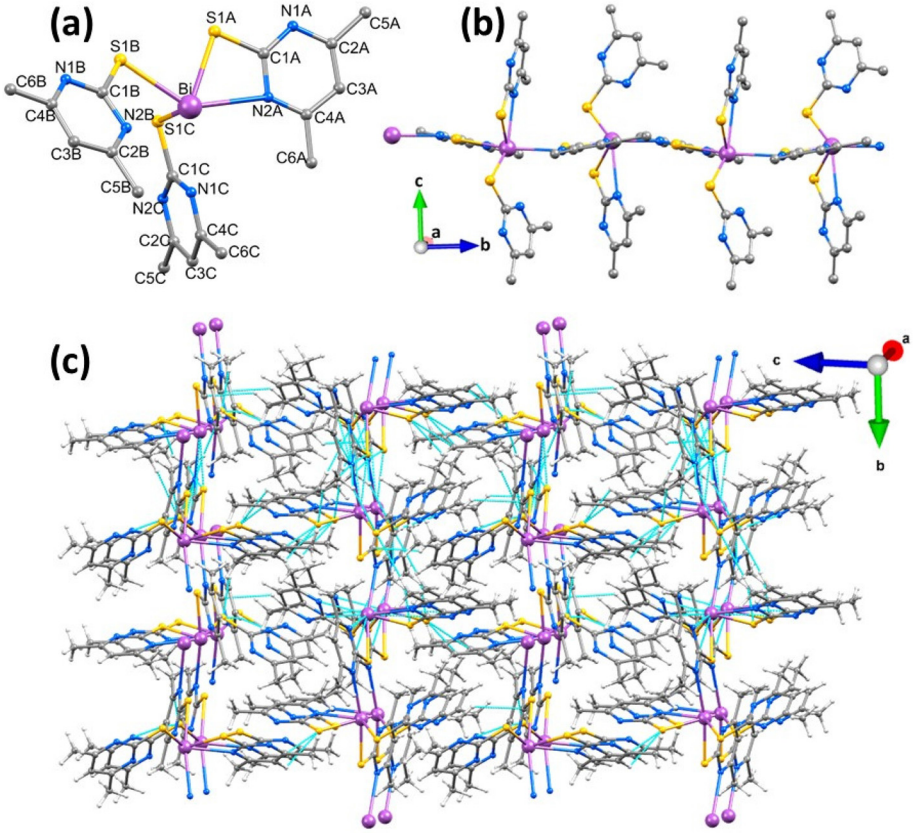

Fig. 2 (a) Molecular structure, (b) 1D polymeric chain and (c) packing diagram of $[Bi(4,6\text{-}Me_2pymS)_3]_n$ (**1**).

cantly longer than that reported in the literature *i.e.*, 2.5815(5) Å in $[Bi(1\text{-}MMTZ)_2\{(PYM)(PYM(H))_2\}]$.[32] In complex **1**, the Bi–N (2B) and Bi–N(1C) bond distances of 2.952 Å and 2.962 Å can be considered as weak interactions since their values are less than the sum of the van der Waals radii (3.62 Å).[29] All three S(1A)–C(1A), S(1B)–C(1B) and S(1C)–C(1C) bond distances (1.75 Å) are well anticipated in the literature reports which reflect the existence of a single bond character, hence confirming the predominance of the thiol form over the thione form.[32]

Thermal studies

Analysis of the thermal behavior of any coordination complex is of utmost importance, especially when the latter is intended to be utilized as a single-source molecular precursor. The experiment was performed on a crystalline sample in the temperature range of 50–800 °C under an N_2 atmosphere with a heating rate of 10 °C min^{-1}. From the TG profile of **1** (Fig. 3), it can be inferred that the complex is stable up to ~310 °C, after which the complex collapses *via* two-step decomposition. The first step of prompt decomposition (observed ~ 18.1%) corresponds to the formation of Bi_2S_3 (calculated ~18.2%). A gradual weight loss up to 800 °C was observed and the final weight loss (observed ~48%) does not correspond to any composition of bismuth sulfide. It is well reported in the literature that the volatile nature and possibility of sublimation at an elevated temperature in group V metal sulfides (V–VI materials) restrict the exact determination of the nature of the residue on the basis of weight loss percentage calculations.[26] Another plausible reason behind this type of gradual weight loss is the polymeric nature of the complex, which is quite

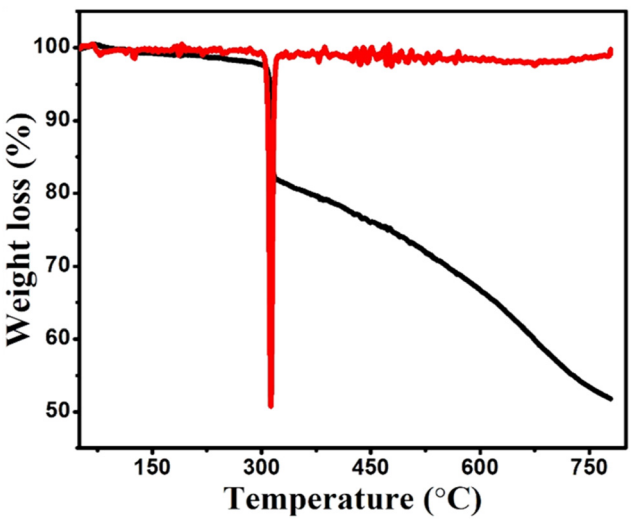

Fig. 3 Thermogravimetric analysis (TGA) curve for $[Bi(4,6\text{-}Me_2pymS)_3]_n$ (**1**).

commonly observed for coordination polymers and MOFs as given in the literature.[33]

Preparation and characterization of bismuth sulfide nanostructures

The thermal analysis of **1** has proved that the complex can be utilized as a suitable single-source precursor for the preparation of bismuth sulfide materials. To further validate this claim, thermolysis of the complex was performed by the heat-up method in oleylamine (OAm). The selection of solvent was done based on the fact that OAm has a high boiling point (350 °C) and acts as a strong capping agent. Moreover, OAm being liquid at room temperature makes the purification procedure of the final product hassle-free. OAm is also known to facilitate the decomposition of the precursor by catalysing the process, thereby bringing down the decomposition temperature as compared to the TGA process.[34] Well-separated nucleation and growth steps are promoted in OAm, which leads to the formation of monodisperse nanoparticles.[35] Revaprasadu *et al.* reported the synthesis of antimony selenide nanorods in OAm at a relatively lower temperature.[36] For temperature optimization, the complex was first heated in OAm by the heat-up method to point out the minimum decomposition temperature. It was found that the complex decomposes at a very low temperature of 130 °C. The reaction was continued for 10 minutes. The PXRD pattern of the isolated material (Fig. 4b) closely matched with phase-pure orthorhombic Bi_2S_3 (bismuthinite) (ICSD Coll. Code 30775, space group: P_{bnm}). The PXRD pattern, however, reveals the predominant formation of only (211) and (150) planes of the materials at 2θ = 26.0° and 46.6°, respectively, with a highly amorphous nature (**BS1**). Thus, it was considered worthwhile to increase the reaction duration at the same temperature in order to investigate the effect of time on the crystallinity of Bi_2S_3. Accordingly, decomposition at 130 °C was performed with a 30 minute reaction time (**BS2**). The PXRD pattern as shown in Fig. 4c shows a similar amorphous nature to that observed in **BS1**. Thus, the increase in reaction duration does not seem to have a drastic effect on the crystallinity of the material; a slight improvement, however, was evident with a recognizable (231) plane in the latter case at 2θ = 52.8°. In the third set of reactions, the reaction temperature was increased to 160 °C and a duration of 10 minutes was considered (**BS3**). The reflections originating from the PXRD pattern of **BS3** can be exactly matched with the same originating from the (002), (012), (022), (011), (111), (210), (211), (122), (130), (131), (024), (123), (104), (114), (002), (150), (231) and (242) planes of the orthorhombic Bi_2S_3 material (Fig. 4d). The strong and sharp PXRD peaks in the case of **BS3** indicate the high crystallinity of Bi_2S_3. In all the cases, the PXRD patterns do not contain any other reflections from any other phases of bismuth sulfide which confirms the phase purity of the nanostructures in all the three cases, while the broadening of the peaks is indicative of nano-sized particle formation. The average crystallite size calculated from the Scherrer equation[37] was found to be ~9, 11.3 and 26 nm for **BS1**, **BS2** and **BS3**, respectively. It is important to mention that the Scherrer equation is often used to estimate the average crystallite size by correlating the scattering domain size and the FWHM (peak broadening) in the PXRD pattern. However, other factors like crystal distortion and defect formation are not considered in the equation.

2D elemental mapping is a quality tool to understand the distribution of constituent elements in any material. The 2D image presented in ESI Fig. S1† shows that Bi and S are distributed uniformly within the nanostructures. To gain better insight into the composition of the as-prepared bismuth

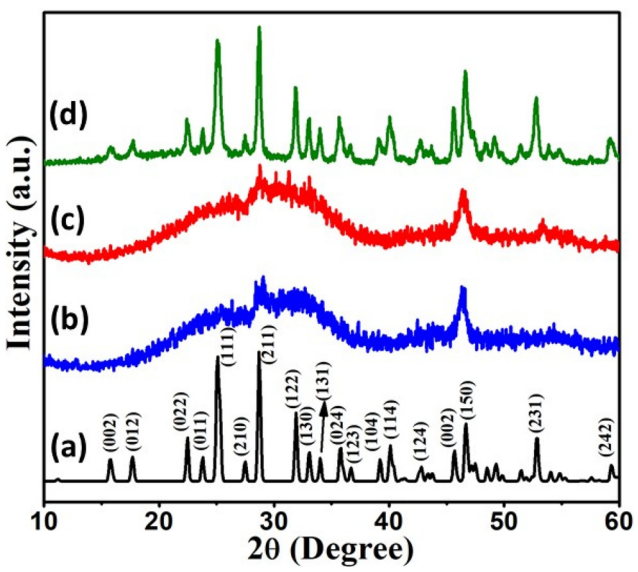

Fig. 4 (a) Simulated powder X-ray pattern (PXRD) of orthorhombic Bi_2S_3 (ICSD Coll. Code 30775). PXRD patterns of Bi_2S_3 synthesized at (b) 130 °C, 10 min (**BS1**), (c) 130 °C, 30 min (**BS2**) and (d) 150 °C, 10 min (**BS3**).

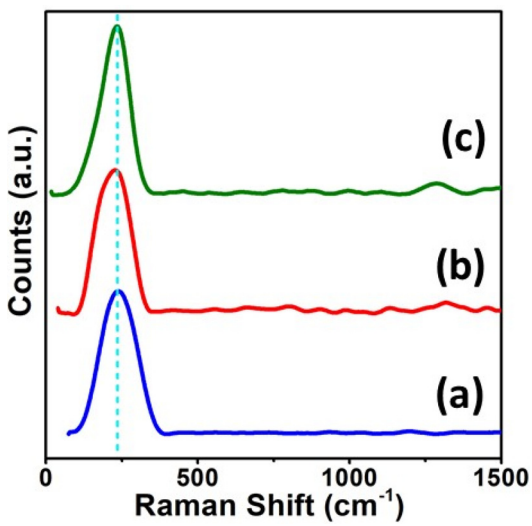

Fig. 5 Raman spectra of Bi_2S_3 synthesized at (a) 130 °C for 10 min (**BS1**), (b) 130 °C for 30 min (**BS2**) and (c) 150 °C, 10 min (**BS3**), respectively.

sulfide nanomaterials, EDS analysis was carried out (ESI Fig. S2†). The EDS spectra revealed that the atomic ratios of Bi and S are 39.8 : 60.2 (2 : 3.02), 38 : 62 (2 : 3.2) and 59.9 : 40.1 (3 : 2) for **BS1**, **BS2** and **BS3**, respectively, confirming the formation of Bi_2S_3 in each case.

Raman spectroscopy is an ideal technique to investigate the phase purity along with the local site symmetry of any nanostructures. Moreover, Raman spectroscopy provides direct insight into the vibrational properties of any crystalline material. Thus, Raman spectroscopy was employed to characterize the Bi_2S_3 nanostructures. The Raman spectra reveal single vibrational mode peaks at 235.8, 236.1 and 235.9 cm^{-1} for **BS1**, **BS2** and **BS3**, respectively, (Fig. 5), which match perfectly with the characteristic of the A_g phonon mode for the Bi_2S_3 material as reported in the literature.[38] From the spectra, it is also seen that there are slight shifts in the Raman peak positions among the Bi_2S_3 nanostructures, which are manifestations of the nano-size effects.[39] Furthermore, as the particle size of the Bi_2S_3 nanostructures increases from **BS1** to **BS3**, a consistent increase in peak broadening (FWHM) is evident which is often observed in materials in the nano-regime and happens due to lattice expansion, confinement of phonons and enhanced phonon–phonon interactions as reported in the literature.[40]

The morphology of the as-prepared Bi_2S_3 nanostructures was investigated by electron microscopy techniques. Fig. 6a represents the SEM image of **BS1**. When corroborated with the TEM image of **BS1** (Fig. 6d), the formation of flocculants with an ill-defined morphology is depicted. From the SEM and TEM images of **BS2** (Fig. 6b and e), which was synthesized at the same temperature but for a longer duration, it is clearly seen that the material comprises irregular nanoflakes. In both these

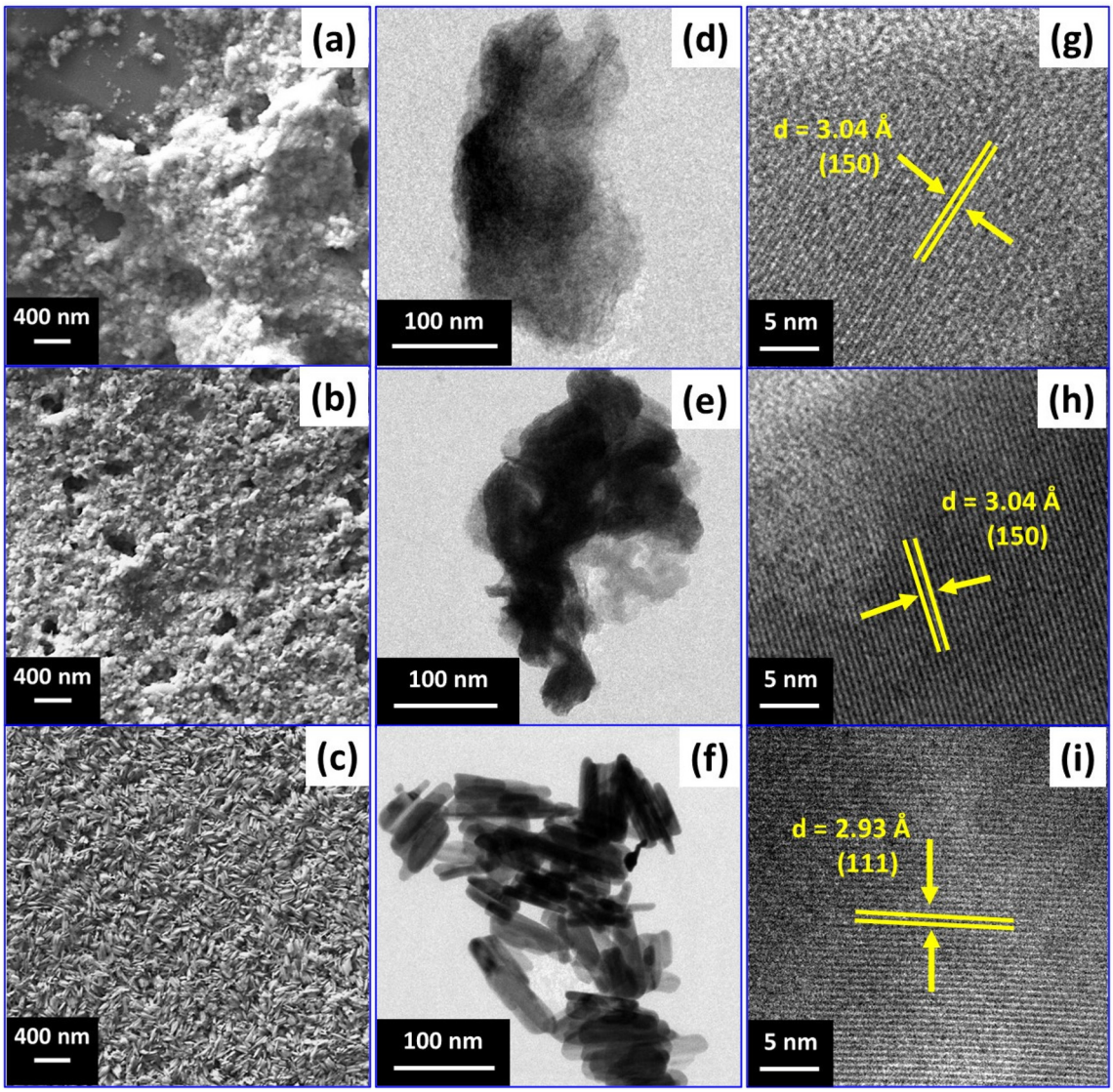

Fig. 6 (a, b and c) SEM micrographs, (d, e and f) TEM images and (g, h and i) HRTEM images of Bi_2S_3 synthesized at 130 °C for 10 min (**BS1**), 130 °C for 30 min (**BS2**) and 150 °C, 10 min (**BS3**), respectively.

scenarios, the HRTEM images shown in Fig. 6g and h for **BS1** and **BS2**, respectively, show the presence of lattice fringes with a clear *d*-spacing of 3.04 Å, which can be indexed to the (150) plane of orthorhombic Bi_2S_3. Finally, the SEM micrograph of the bismuth sulfide synthesized at a higher temperature (**BS3**) reveals the presence of uniformly distributed small "rice grain" shaped nanorods (Fig. 6c). The TEM image (Fig. 6f) further confirms the nanorod morphology. The corresponding HRTEM reveals a *d*-spacing of 2.93 Å, which is indexed to the (111) plane (Fig. 6i). From the above discussion, interestingly, it can be realized that by the utilization of the precursor under study, size and morphology modulation in bismuth sulfide nanostructures can be effortlessly achieved with subtle variations in thermolysis conditions.

Furthermore, the HRTEM images and the corresponding *d*-spacing values also support the growth of differently shaped bismuth sulfides. Xu *et al.*, in a recent article, demonstrated that the preferential growth of the bismuth sulfide material along the (015) direction favours the formation of a 2-dimensional morphology (nanoflakes in the case of **BS2**).[41] A similar investigation by Sharma *et al.* has also led them to the same conclusion.[42] In contrast, several studies, including a recent one from Onwudiwe's group,[43] have proved that the formation of 1D nanostructures (nanorods in the case of **BS3**) is evident when the growth is directed along either the (111) or (211) plane. The growth of 1-dimensional nanorods can be understood on the basis of the orientation of Bi and S in the lattice. The lamellar arrangement of Bi^{3+} and S^{2-} in the infinite chain structure, joined together by weak Bi–S bonds, imparts anisotropic nature to the structure. The crystal structure of Bi_2S_3 is composed of such infinite one-dimensional long chains which are interconnected by weak van der Waals forces of attraction as shown in Fig. 7.[44] These weak interactions disappear at higher temperatures (in the present case, 150 °C), leading to the separation of chains which facilitates the formation of 1D nanostructures.[26]

Optical properties

Bismuth sulfide is a non-toxic crystalline n-type compound semiconductor belonging to the V–VI semiconductor material family. Bulk Bi_2S_3 features a narrow band gap of 1.4 eV.[45] This feature of Bi_2S_3, when combined with its high absorption coefficient (10^{-4} to 10^{-6} cm^{-1}),[46] makes it a fine candidate for optoelectronics, photovoltaics, and a good photocatalyst that is able to perform in the visible range of the solar spectrum. Keeping in mind the importance of optical band gaps in nanoelectronics, the optical properties of Bi_2S_3 nanostructures were investigated by diffuse reflectance spectroscopy (DRS) and the optical band gaps of these materials were determined by plotting the Kubelka–Munk function, $F(R)$, as given in the following equation:

$$[F(R)h\nu]^n = A(h\nu - E_g)$$

where $h\nu$ is the photon energy, A is a constant, E_g denotes the band gap, and n depends on the nature of the optical transition. The direct band gap of the materials was calculated using Tauc's model ($n = 2$).

From the diffuse reflectance spectra given in Fig. 8, it is observed that the direct optical band gaps of Bi_2S_3 nanostructures are 2.15, 2.00 and 1.93 eV for **BS1**, **BS2** and **BS3**, respectively. These values are clearly blue shifted with respect to the bulk band gap. The tunability in the band gap value in the as-prepared nanostructures is a function of the increasing average crystallite size as we move from **BS1** to **BS3** since it is a well-known fact that with increasing size, the optical band gap

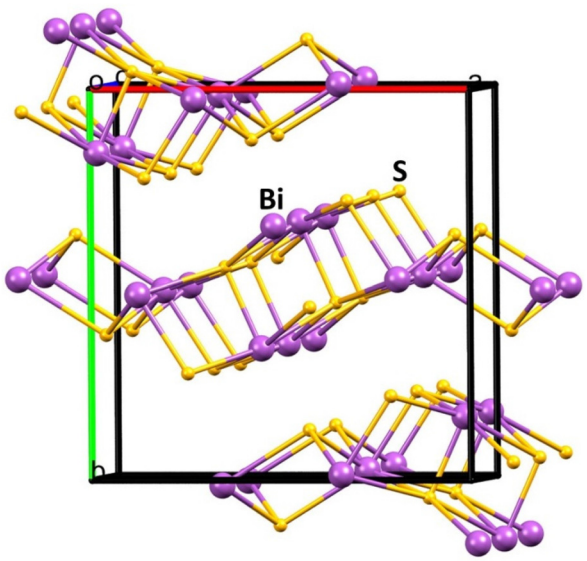

Fig. 7 Perspective view of the crystal structure of orthorhombic Bi_2S_3 (ICSD Coll. Code 30775).

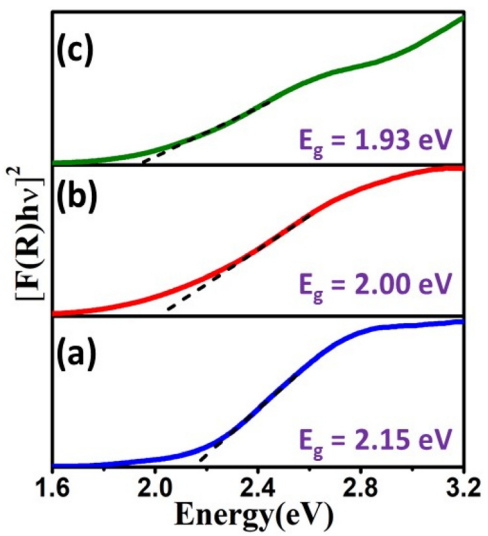

Fig. 8 Plots of $[F(R)h\nu]^2$ *vs.* energy generated by the Kubelka–Munk transformation of solid-state diffuse reflectance data of Bi_2S_3 synthesized at (a) 130 °C for 10 min (**BS1**), (b) 130 °C for 30 min (**BS2**) and (c) 150 °C, 10 min (**BS3**), respectively.

decreases.[47] The probable reason for the blue shift of the band gaps may be lattice distortions, surface lattice defects, quantum confinement or the surface effect of the carriers.[48]

Considering the fact that Bi_2S_3 has a large excitonic Bohr radius (r_B) ~ 24 nm[49] and that the average crystallite sizes of **BS1** and **BS2** are lower than the above value, it would be reasonable to consider the presence of quantum confinement effects in **BS1** and **BS2**. However, in the case of **BS3**, due to its large average size, the presence of quantum confinement can be ruled out and the observed blue shift in the optical band gap may be attributed to lattice distortion or surface lattice defects. Nevertheless, the correlation between the size and optical band gap observed in the current study is in agreement with literature reports. For instance, Xiao *et al.* reported a band gap of 1.9 eV for Bi_3S_3 nanorods with an average diameter of ~15 nm.[50] In a separate study, Gao *et al.* fabricated morphology-controlled Bi_3S_3 nanostructures with band gap tunability. They have isolated hexagonal plates, mesocrystalline sheets and nanowires of Bi_3S_3 with optical band gaps of 1.54, 1.73 and 1.96 eV, respectively.[51]

Furthermore, the density of states and band structure of Bi_3S_3 were calculated considering a conventional unit cell containing 20 atoms (8 Bi, 12 S) (ESI Fig. S3†). Fig. 9a presents the calculated projected density of states (PDOS) and band structure of Bi_2S_3. The calculated band gap is found to be around 1.25 eV which is quite close to the experimentally observed value of bulk Bi_2S_3 (~1.4 eV).[45] The valence band maxima (VBM) and conduction band minima (CBM) are located along the Γ–Y/ Γ–X directions (Fig. 9b). The PDOS near the valence band maxima consist of majorly S-3p orbitals along with minor contributions from Bi-6s and Bi-6p states. In contrast, the conduction band minima have major contributions from the mixed states of Bi-6p, S-3s and S-3p orbitals. Overall, the S-state dominates the VBM while the Bi-state dominates the CBM. Thus, optical transitions from the valence band to the conduction band are expected to originate from the S-state and terminate in the Bi-state, which is consistent with the fact that each Bi is surrounded by seven S atoms within the 3.4 Å separation distance.

Photo-response and photo-switching study of Si/Bi_2S_3 liquid-junction photoelectrochemical cells

Bi_2S_3 is one of the earliest materials known to exhibit photoconducting properties.[6] The photo-response and photo-switching behaviours of the as-prepared Bi_2S_3 have been evaluated by fabricating prototype photoelectrochemical (PEC) cells with a three-electrode system. The working electrode was fabricated by spin coating a colloidal suspension of Bi_2S_3 nanomaterials in toluene over a Si substrate followed by evaporation of the solvent to obtain a thin film of the material. Experimental details are provided in the ESI.†

In the present work, since phase-pure Bi_2S_3 has been isolated in all the three reactions, **BS3** was selected as a representative material keeping in mind the good crystallinity and band gap, and the photo-response and photo-switching of this material were investigated. The current–voltage (*I–V*) measurement for the Si/Bi_2S_3 cell shows a nonlinear characteristic when irradiated in the presence of Na_2S and Na_2SO_3 as electrolytes (Fig. 10a). Upon illuminating with a light source (200 μW cm^{-2}), the energy from the light excites the electrons in the semiconductor Bi_2S_3 from the valence band into the conduction band. This increase in the availability of electrons results in increased photoconductivity (Fig. 10b), which shows the photo-response as a function of time when the lamp was switched on and off. The cell shows no further change in current upon exposing to light after a considerable amount of time which indicates a saturation process. When the light is turned off, the "carrier generation process" abruptly stops, while the "carrier loss process" continues, resulting in a sudden decrease in conductivity.[52] Thus, the cell made from the Bi_2S_3 nanomaterial, under dark and light conditions, shows good photo-switching and photostability between low and high conductivity. Guo *et al.* reported earlier that resistive switching in Bi_2S_3 occurs due to its specific intrinsic doping

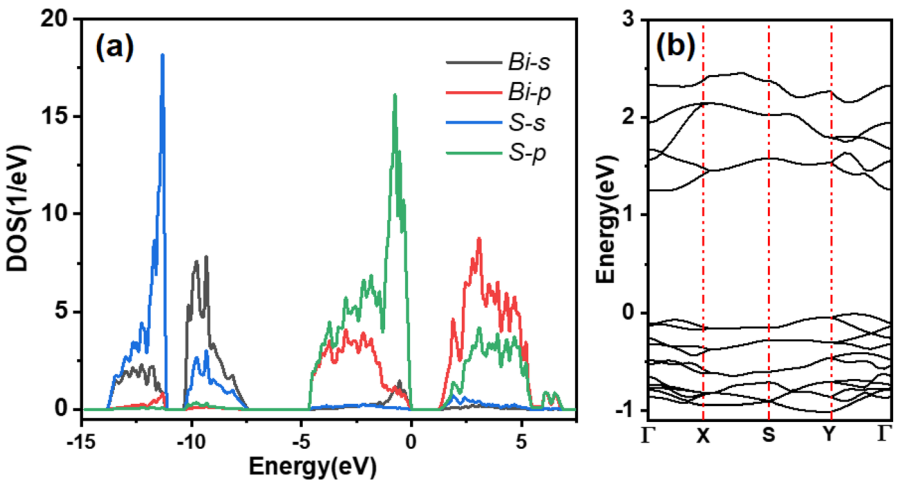

Fig. 9 (a) Projected density of states and (b) the band structure of Bi_2S_3.

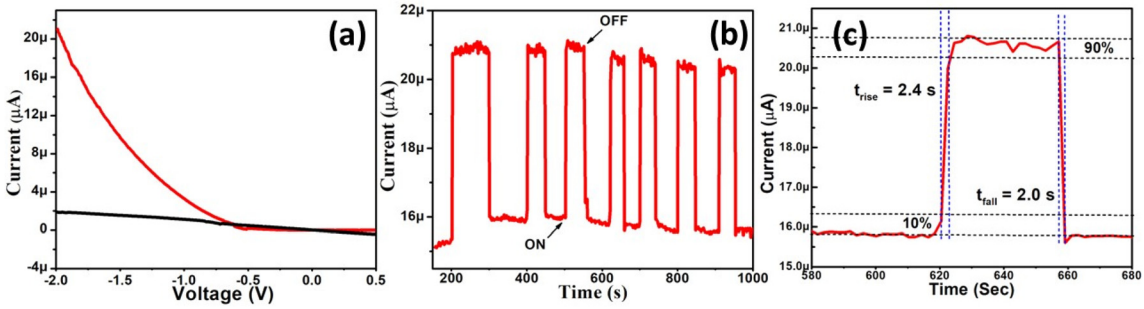

Fig. 10 (a) *I–V* characteristics, (b) reversible switching behaviour under alternating light and dark conditions and (c) an expanded view of the middle cycle of the pristine Bi_2S_3 nanorods synthesized at 150 °C, 10 min (**BS3**).

with sulfur vacancies and hence it exhibits great potential for application in resistive memory devices.[53] Here on applying a bias voltage of −1.5 V, the photocurrent ($I_{pc} = I_{light} - I_{dark}$) is found to be ∼5 μA while in an earlier report, Bi_2S_3 nanowires synthesized by Bao *et al.* using the hydrothermal method showed photocurrents of ∼60 nA and ∼20 nA when illuminated using a green laser and a quartz lamp as light sources, respectively, and with a bias voltage of 3 V.[54] Later, Xiao *et al.*[50] reported Bi_2S_3 hierarchical architectures which exhibited an improved photocurrent of ∼28 μA on applying a bias voltage of 5 V, which is significantly higher compared to the bias voltage used in the present study. Photoresponsivity is the photocurrent generation efficiency of any material and can be expressed by the ratio of generated photocurrent and incident optical power ($R = I_{pc}/PS$)[55] (P = 200 μW cm^{-2} and the effective area of the cell S = 0.785 cm^2 in the present case). In this study, the photoresponsivity was calculated to be 31 mA W^{-1}. From the repeated cycles, the middle cycle has been chosen to calculate the rise time (the time required for the current to increase from 10% to 90% of the peak value) and fall time in each case. The rise and fall times for **BS3** are 2 s, indicating fast response (Fig. 10c). It is to be noted that the rise and fall times are the same in this case, which indicates the involvement of fewer trap states or defects in the switching process.[56] The fast switching characteristics along with good photoresponsivity obtained in the present study for Bi_2S_3 nanorods prove their candidature as a low-cost alternative photon absorber material for solar cells as well as an efficient material for photodetectors and optical switches.

Conclusion

This study describes the successful room temperature synthesis and structural characterization of a stable bismuth-dimethylpyrimidylthiolate molecular precursor for Bi_2S_3 nanostructures. Notably, the three dimethylpyrimidylthiolate ligands attached to the bismuth centre exhibit different kinds of coordination behaviors, which leads to the isolation of a 1D $[Bi(\kappa\text{-S,N-pymS})(pymS)(\mu\text{-S,N-pymS})]_n$ polymeric chain. The complex undergoes facile thermal transformation to afford phase-pure Bi_2S_3 nanostructures at low temperatures in OAm. Interestingly, the reaction temperature was significantly lower than the decomposition temperature of the complex as determined by TGA. This clearly reflects that OAm not only serves as a capping agent for the nanostructures but also catalyzes the decomposition of the precursor. Additionally, the investigation also highlighted the significant influence of the reaction temperature on the phase formation, morphology and bandgap of the nanostructures. The estimated bandgaps of the nanostructures were blue shifted with respect to the bulk bandgap and are in the range suitable for solar cell applications. Furthermore, the prototype photo-electrochemical cell fabricated from the pristine Bi_2S_3 nanostructures exhibited remarkable photoresponsivity and photostability under alternating light and dark conditions. Overall, this report presents a facile and scalable route to Bi_2S_3 nanostructures at relatively low temperatures with the liberty of tuning the morphology and bandgap. A similar approach can be explored for other metals to develop efficient precursors in the future for the preparation of high-quality metal chalcogenide nanostructures.

Conflicts of interest

The authors declare no conflicts of interest.

Acknowledgements

We thank Dr A. K. Tyagi, Director, Chemistry Group, Bhabha Atomic Research Centre for encouraging this work. We also thank Dr Bal Govind Vats (Fuel Chemistry Division, Bhabha Atomic Research Centre) for TG and PXRD measurements. RJB acknowledges with sincere gratitude the Advanced Photon Source (APS) located at the Argonne National Laboratory for mounting the crystal at their facility. Chem Mat CARS Sector 15 is supported by the National Science Foundation under grant number NSF/CHE-1834750. This research used resources of the Advanced Photon Source, a U.S. Department of Energy (DOE) Office of Science User Facility operated for the DOE Office of Science by the Argonne National Laboratory under Contract No. DE-AC02-06CH11357.

References

1 A. Swarnkar, W. J. Mir, R. Chakraborty, M. Jagdeeswararao, T. Sheikh and A. Nag, *Chem. Mater.*, 2019, **31**, 565–575.
2 D. Wang, F. Yin, Z. Du, D. Han and J. Tang, *J. Mater. Chem. A*, 2019, **7**, 26205–26226.
3 G. Karmakar, A. Tyagi, A. P. Wadawale, A. Y. Shah, G. Kedarnath, A. P. Srivastava and V. Singh, *J. Mater. Sci.*, 2020, **50**, 15439–15453.
4 A. A. Tahir, M. A. Ehsan, M. Mazhar, K. G. U. Wijayantha, M. Zeller and A. D. Hunter, *Chem. Mater.*, 2010, **22**, 5084–5092.
5 W. M. Linhart, S. J. Zelewski, P. Scharoch, F. Dybala and R. Kudrawiec, *J. Mater. Chem. C*, 2021, **9**, 13733–13738.
6 M. Bernechea, Y. Cao and G. Konstantatos, *J. Mater. Chem. A*, 2015, **3**, 20642–20648.
7 J. Chen, S. Qin, G. Song, T. Xiang, F. Xin and X. Yin, *Dalton Trans.*, 2013, **42**, 15133–15138.
8 C. Nithya, J. K. R. Modigunta, I. In, S. Kim and S. Gopukumar, *ACS Appl. Nano Mater.*, 2023, **6**, 6121–6132.
9 L. X. Hao, G. Chen, Y. G. Yu, Y. S. Zhou, Z. H. Han and Y. Liu, *Int. J. Hydrogen Energy*, 2014, **39**, 14479–14486.
10 M. P. Motaung, D. C. Onwudive and W. Lei, *ACS Omega*, 2021, **6**, 18975–18987.
11 B. Sun, T. Feng, J. Dong, X. Li, X. Liu, J. Wu and S. Ai, *CrystEngComm*, 2019, **21**, 1474–1481.
12 V. Brune, M. Grosch, R. Weibing, F. Hartl, M. Frank, S. Mishra and S. Mathur, *Dalton Trans.*, 2021, **50**, 12365–12385.
13 D. C. Onwudiwe and V. M. Nkwe, *Heliyon*, 2020, **6**, e04505.
14 W. N. Kun, S. Mlowe, L. D. Nyamen, M. P. Akerman, P. O'Brien, P. T. Ndifon and N. Revaprasadu, *Polyhedron*, 2018, **154**, 173–181.
15 W. N. Kun, S. Mlowe, L. D. Nyamen, P. T. Ndifon, M. A. Malik, O. Q. Munro and N. Revaprasadu, *Chem. – Eur. J.*, 2016, **22**, 13127.
16 W. N. Kun, P. D. McNaughter, L. D. Nyamen, B. F. Spencer, P. O'Brien, P. T. Ndifon and N. Revaprasadu, *RSC Adv.*, 2019, **9**, 15836–15844.
17 O. C. Monteiro, T. Trindade, J. H. Park and P. O'Brien, *Chem. Vap. Deposition*, 2000, **6**, 230–232.
18 Q. Han, J. Chen, X. Yang, L. Lu and X. Wang, *J. Phys. Chem. C*, 2007, **111**, 14072–14077.
19 L. Tian, H. Y. Tan and J. J. Vittal, *Cryst. Growth Des.*, 2008, **8**, 734–738.
20 J. L. T. Chen, V. Nalla, G. Kannaiyan, V. Mamidala, W. Ji and J. J. Vittal, *New J. Chem.*, 2014, **38**, 985–992.
21 T. Alqahtani, M. D. Khan, D. J. Kelly, S. J. Haigh, D. J. Lewis and P. O'Brien, *J. Mater. Chem. C*, 2018, **6**, 12652–12659.
22 W. Lou, M. Chen, X. Wang and W. Liu, *Chem. Mater.*, 2007, **19**, 872–878.
23 M. Y. Masoomi and A. Morsali, *Coord. Chem. Rev.*, 2012, **256**, 2921–2943.
24 K. J. Lee, J. H. Lee, S. Jeoung and H. Moon, *Acc. Chem. Res.*, 2017, **50**, 2684–2692.
25 G. Karmakar, A. Tyagi, K. K. Halankar, S. Nigam, B. P. Mandal, A. P. Wadawale, G. Kedarnath and A. K. Debnath, *Dalton Trans.*, 2023, **52**, 1461–1475.
26 A. Thomas, G. Karmakar, A. Y. Shah, S. V. Lokhande, A. Y. Kulkarni, A. Tyagi, R. S. Chauhan, N. N. Kumar and A. P. Singh, *Dalton Trans.*, 2022, **51**, 12181–12191.
27 G. Karmakar, A. Tyagi, A. Y. Shah, S. Nigam, A. P. Wadawale, G. Kedarnath, B. G. Vats, N. N. Kumar and V. Singh, *Dalton Trans.*, 2022, **51**, 12670–12685.
28 A. Tyagi, G. Karmakar, B. P. Mandal, D. D. Pathak, A. Wadawale, G. Kedarnath, A. P. Srivastava and V. K. Jain, *Dalton Trans.*, 2021, **50**, 13073–13085.
29 R. K. Sharma, G. Kedarnath, V. K. Jain, A. Wadawale, M. Nalliath, C. G. S. Pillaia and B. Vishwanadh, *Dalton Trans.*, 2010, **39**, 8779–8787.
30 E. Wächtler, R. Gericke, T. Block, B. Gerke, R. Pöttgen and J. Wagler, *Z. Naturforsch., B: J. Chem. Sci.*, 2021, **76**, 103–118.
31 E. Block, G. O. Okai, H. Kang, J. Wu and J. Zubieta, *Inorg. Chem.*, 1991, **30**, 4784–4788.
32 A. Luqman, V. L. Blair, R. Brammananth, P. K. Crellin, R. L. Coppel and P. C. Andrews, *Eur. J. Inorg. Chem.*, 2016, **2016**, 2738–2749.
33 A. Walczak, G. Kurpik and A. R. Stefankiewicz, *Int. J. Mol. Sci.*, 2020, **21**, 6171.
34 S. Mourdikoudis and L. M. L. Marzan, *Chem. Mater.*, 2013, **25**, 1465–1476.
35 Y. C. Cao and J. Wang, *J. Am. Chem. Soc.*, 2004, **126**, 14336–14337.
36 M. D. Khan, M. Aamir, M. Sohail, M. Sher, J. Akhtar, M. A. Malik and N. Revaprasadu, *Sol. Energy*, 2018, **169**, 526–534.
37 P. Scherrer, *Nachr. Ges. Wiss. Goettingen, Math.-Phys. Kl.*, 1918, **2**, 98–100.
38 M. P. Deshpande, P. N. Sakariya, S. V. Bhatt, N. H. Patel, K. Patel and S. H. Chaki, *Bull. Mater. Sci.*, 2015, **38**, 83–88.
39 U. V. Ghorpade, M. P. Suryawanshi, S. W. Shin, I. Kim, S. K. Ahn, J. H. Yun, C. Jeong, S. S. Kolekar and J. H. Kim, *Chem. Mater.*, 2016, **28**, 3308–3317.
40 O. A. Yassin, S. N. Alamri and A. A. Joraid, *J. Phys. D: Appl. Phys.*, 2013, **46**, 235301.
41 X. Xu, C. Ye, D. Chao, B. Chen, H. Li, C. Tang, X. Zhong and S.-Z. Qiao, *Adv. Mater.*, 2022, **34**, 2108688.
42 A. Sharma, B. Bhattacharyya, A. K. Srivastava, T. D. Senguttuvan and S. Husale, *Sci. Rep.*, 2016, **6**, 19138.
43 T. O. Ajiboye and D. C. Onwudiwe, *Results Chem.*, 2021, **3**, 100151.
44 C. Li, J. Zhao, Q. Hu, Z. Liu, Z. Yu and H. Yan, *J. Alloys Compd.*, 2016, **688**, 329–335.
45 T. O. Ajiboye, O. A. Oyewo and D. C. Onwudiwe, *Surf. Interfaces*, 2021, **23**, 100927.
46 T. Fazal, S. Iqbal, M. Shah, A. Bahadur, B. Ismail, H. S. M. Abd-Rabboh, R. Hameed, Q. Mahmood, A. Ibrar, M. S. Nasar, Y. Ehsan, A. N. S. Saqib, Adnan and M. A. Qayyum, *J. Mater. Sci.: Mater. Electron.*, 2022, **33**, 42–53.

47 G. Karmakar, A. Tyagi, A. Wadawale, G. Kedarnath, A. P. Srivastava, C. A. Betty and V. Singh, *ChemistrySelect*, 2018, **3**, 10394–10401.
48 G. Karmakar, D. D. Pathak, A. Tyagi, B. P. Mandal, A. Wadawale and G. Kedarnath, *Dalton Trans.*, 2023, **52**, 6700–6711.
49 E. V. Guimarães, E. R. Gonçalves, S. A. Lourenço, L. C. Oliveira, O. Baffa, A. C. A. Silva, N. O. Dantas and R. S. Silva, *J. Alloys Compd.*, 2018, **740**, 974–979.
50 G. Xiao, Q. Dong, Y. Wang, Y. Sui, J. Ning, Z. Liu, W. Tian, B. Liu, G. Zou and B. Zou, *RSC Adv.*, 2012, **2**, 234–240.
51 M.-R. Gao, S.-H. Yu, J. Yuan, W. Zhang and M. Antonietti, *Angew. Chem., Int. Ed.*, 2016, **55**, 12812–12816.
52 G. Karmakar, A. Tyagi, A. Y. Shah, L. B. Kumbhare, A. P. Wadawale, G. Kedarnath and V. Singh, *RSC Adv.*, 2022, **12**, 27292–27299.
53 D. Guo, C. Hu and C. Zhang, *Mater. Res. Bull.*, 2013, **48**, 1984–1988.
54 H. Bao, X. Cui, C. M. Li, Y. Gan, J. Zhang and J. Guo, *J. Phys. Chem. C*, 2007, **11**, 12279–12283.
55 Q. Hao, J. Liu, G. Wang, J. Chen, H. Gan, J. Zhu, Y. Ke, Y. Chai, J. Lin and W. Zhang, *ACS Nano*, 2020, **14**, 11373–11382.
56 G. Karmakar, A. Y. Shah, A. Tyagi, A. P. Wadawale, G. Kedarnath, N. N. Kumar and J. Bahadur, *New J. Chem.*, 2022, **46**, 3871–3881.